Neutron capture reactions relevant to the *s* and *p* processes in the region of the $N = 50$ shell closure

Saumi Dutta,* G. Gangopadhyay,† and Abhijit Bhattacharyya‡
Department of Physics, University of Calcutta, 92 Acharya Prafulla Chandra Road, Kolkata 700 009, India
(Received 19 April 2016; revised manuscript received 9 July 2016; published 4 August 2016)

The radiative neutron capture cross sections for nuclei participating in the *s*-process and the *p*-process nucleosynthesis in and around the $N = 50$ closed neutron shell have been calculated in a statistical semimicroscopic Hauser-Feshbach approach for the energy range of astrophysical interest. A folded optical-model potential is constructed utilizing the standard DDM3Y real nucleon-nucleon interaction. The folding of the interaction with target radial matter densities, obtained from the relativistic mean-field theory, is done in coordinate space using the spherical approximation. The standard nuclear reaction code TALYS1.8 is used for cross-section calculation. The cross sections are compared with experimental results. Maxwellian-averaged cross sections and astrophysical reaction rates for a number of selected nuclei are also presented.

DOI: 10.1103/PhysRevC.94.024604

I. INTRODUCTION

Elements heavier than iron are produced via two principal processes, namely, the slow neutron capture process (*s*-process) and the rapid neutron capture process (*r*-process), differing in the respective neutron capture time scales with respect to the β-decay half-lives. There is a minor contribution from another process, namely, the *p*-process, producing a subset of proton-rich isotopes. The detailed study of heavy element nucleosynthesis was done in the fundamental work of Burbidge *et al.* [1] and also of Cameron [2].

While the majority of the theory of the *s*-process is well-developed, uncertainty still remains in constraining the neutron capture rates. The capture cross sections are highly scattered and uncertain in the energy range appropriate for astrophysical applications. Moreover, the reaction cross sections for some important nuclei are still not available due to their unavailability in the terrestrial laboratory. Käppeler *et al.* [3] showed the present status of the uncertainty of stellar (n,γ) cross sections and commented that improvements are certainly necessary especially in the mass region below $A = 120$ and above $A = 180$. Nuclei with closed neutron shells act as bottlenecks to the *s*-process reaction flow due to their low cross sections. The cross sections for the branch-point nuclei also have to be known with better accuracy because the branching analysis in the *s*-process path can give valuable information on various constraints about the astrophysical medium.

The *s*-process is subdivided into weak, main, and strong components. Recently, another component, called the lighter element primary process (LEPP), has also been proposed. The weak component occurs during the convective He core and C-shell burning in massive stars driving the material with masses $56 < A < 90$, in contrast to the main component, occurring mostly in asymptotic giant branch (AGB) stars. However, there remains some confusion about the border between these two components, and most of the nuclei considered in the present study reside in the vicinity of this border region. For example, 50% of the solar abundances of the *s*-only pair ^{86,87}Sr are formed in the main component and the remaining 50% are from the weak component of the *s*-process [3].

The present study also involves some nuclei produced in the astrophysical *p*-process near the $N = 50$ closed shell (^{84}Sr, ^{92,94}Mo, ^{96,98}Ru). The (n,γ) reactions have significant impact on *p*-process abundance determination as they hinder the flux by competing with (γ,n) reactions. The (n,γ) cross sections for *p* nuclei are difficult to measure because they are not found in significant amounts for time-of-flight (TOF) or activation measurements and hence, most of the rates are to be inferred from statistical model calculations. In the domain of the $N = 50$ shell proximity, some nuclei exist which are predominantly produced via the *s*-process only. These so called *s*-only isotopes (^{86}Sr, ^{88}Sr, and ^{96}Mo) are of special importance since they can provide necessary clues to the *s*-process branchings.

Though the neutron capture cross sections, in general, have $1/v$ dependence, this can significantly differ when the *p*-wave capture is superimposed on a pure *s*-wave contribution, thus resulting in an increase in the cross-section values with incident neutron energy.

In the next section, we will discuss the theoretical background of our calculation. Then, in Sec. III, we will discuss the results obtained from our theoretical approach. The total (n,γ) cross sections and Maxwellian-averaged cross section (MACS) values for nuclei near the $N = 50$ closed shell, those that take part in the nucleosynthesis chain, are calculated and compared with available experimental data. Lastly, a summary is presented.

In our previous work [4], we employed the present model to calculate the (n,γ) reaction cross sections for nuclei taking part in the *s*-process near the $N = 82$ neutron shell closure. In the current work, we calculate the (n,γ) cross sections and astrophysical reaction rates near the $N = 50$ closed neutron shell. The aim of our work is to construct a consistent framework from the theoretical viewpoint and at the same time test the applicability and feasibility of the model by comparing it with the available measurements so that it can be extended to those regimes which are out of the reach of present-day experiments.

*saumidutta89@gmail.com
†ggphy@caluniv.ac.in
‡abhattacharyyacu@gmail.com

II. THEORY

A. Microscopic statistical model approach for cross-section calculation

We have constructed a microscopic optical-model potential by the folding DDM3Y nucleon-nucleon interaction with the radial matter density of the target, obtained from relativistic mean-field (RMF) theory. The DDM3Y interaction at a scalar distance r for density ρ has the following form:

$$v(r,\rho,E) = t^{M3Y}(r,E)g(\rho). \quad (1)$$

Here $g(\rho)$ is the density-dependent factor. E is the projectile energy in center-of-mass frame. The M3Y interaction (t^{M3Y}) is also supplemented with a zero range pseudopotential. The details can be found in Ref. [4]. This interaction is then folded with target radial matter density and numerical integration is done over the entire volume of the nucleus in coordinate space. Spherical symmetry is assumed.

$$V_{\rm fold}(\mathbf{r},E) = \int v|(\mathbf{r}-\mathbf{r}',\rho,E)|\rho(\mathbf{r}')d\mathbf{r}'. \quad (2)$$

This folded potential $V_{\rm fold}$ is then multiplied by suitable normalization constants $A_{\rm real}$ and $A_{\rm im}$, for the real and imaginary parts, respectively, to construct the optical model potential

$$V_{\rm OMP} = A_{\rm real}V_{\rm fold} + iA_{\rm im}V_{\rm fold}. \quad (3)$$

We have varied the normalization constants $A_{\rm real}$ and $A_{\rm im}$ to have reasonable agreements between the calculated and experimental cross-section values. For radiative proton capture reactions we have observed that the values of $A_{\rm real}$ and $A_{\rm im}$ vary within the order of unity for different mass regions [5–11]. In contrast, we find that around the energy relevant to the s-process, neutron capture reactions can be reasonably well described with $A_{\rm real} = A_{\rm im} = 1$. Variation of the parameters does not improve the overall agreement. Changes in the parameters may improve agreement in each individual reaction. However, as we are more interested in creating a single framework which works for all neutron capture reactions so that we can extend it to yet unstudied cases, we have considered these parameters to be fixed to the above values for all the nuclei.

Energy dependence, particularly in the imaginary part of the potential, is significant near the threshold of new channel openings. This work deals with a very low projectile energy range where only neutron capture and elastic scattering channels are important. A linear energy dependence is embedded in the zero range pseudopotential part of the M3Y interaction [4]. The spin-orbit interaction term is also coupled with phenomenological potential well depths which are the functions of energy [4]. As the energy range studied in the present work is small, the weak energy dependence in the interaction is sufficient to explain the reactions.

The cross sections are calculated using the statistical model reaction code TALYS1.8 [12,13] with the above potential. The Hauser-Feshbach (HF) formalism assumes a large number of resonances at compound formation energy so that the width of an individual one can be averaged over the resonances. This, in turn, requires a high level density in the compound nuclear state in the specified energy window. Targets with closed shells, in general, have widely spaced nuclear levels. The reactions near the shell closure are characterized by small Q values. Hence, here the cross sections are basically dominated by isolated or narrow resonances. In extreme cases, the direct component can also be important and interference terms may also contribute. However, their contribution is too small compared to compound nuclear cross sections and thus, the suppression, in general, does not result in significant error in the calculation. Here, we aim to test the validity and applicability of our model near the shell closures. Our model has already been found to predict the neutron capture cross sections reasonably well at s-process temperatures near the closed shell at $N = 82$ [4]. We have chosen the level density from the microscopic calculation of Goriely *et al.* [14] in the combinatorial method. Goriely *et al.* provided appropriate renormalization factors so that their model can efficiently reproduce the s- and p-wave neutron resonance spacings. Thus, their model has a further advantage that the data can be extrapolated at sufficiently low energies relevant to the neutron capture process, as in the present case of our study.

For radiative capture reactions, the dominant transition that appears in the photon transmission coefficient is of the $E1$ type. This is given by

$$T_{E1} = 2\pi f_{E1}(E_\gamma)E_\gamma^3, \quad (4)$$

where $f_{E1}(E_\gamma)$ is the $E1$ γ-ray strength function dependent on γ-ray energy E_γ and also on the strength, energy, and width of the giant dipole resonances. It is taken from the microscopic Hartree-Fock-Bogoliubov calculations [15] for the present work.

In any reaction mechanism, different channels with their own partial widths are activated depending upon the energy of the system. Hence, the transmission coefficients must be renormalized by suitable multiplication factors. This is taken care of by the width fluctuation correction. It is more important near the threshold of new channel openings where channel strengths differ by large factors. Pairing energy correction for pre-equilibrium reactions is also included. More details can be found in Ref. [4].

For neutron induced reactions, the location of the energy window depends on the contribution from partial waves. A simple approximation is done for the energy peak E_0 and

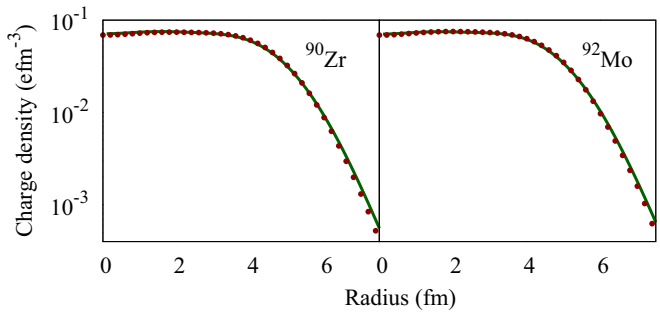

FIG. 1. Charge-density profiles from theoretical RMF model (green solid line) compared with experimental density distributions obtained from Fourier-Bessel parameter fitting (red points) of elastic electron scattering distribution [22].

TABLE I. Binding energy (MeV) and charge radius (fm) values extracted from the RMF theory are compared with experimental data for nuclei in and around the $N = 50$ shell closure. Experimental values for binding energy and charge radius are from Refs. [19,20], respectively.

Nucleus	Binding energy		Charge radius		Nucleus	Binding energy		Charge radius		Nucleus	Binding energy		Charge radius	
	Expt.	Theory	Expt.	Theory		Expt.	Theory	Expt.	Theory		Expt.	Theory	Expt.	Theory
^{82}Kr	714.22	712.33	4.192	4.142	^{83}Kr	721.68	720.00	4.187	4.148	^{84}Kr	732.22	730.74	4.188	4.153
^{86}Kr	749.23	747.31	4.184	4.165	^{85}Rb	739.24	739.20	4.204	4.176	^{84}Sr	728.87	725.29	4.239	4.189
^{86}Sr	748.88	745.98	4.201	4.198	^{87}Sr	757.33	756.16	4.225	4.203	^{88}Sr	768.41	766.13	4.224	4.208
^{89}Y	775.46	774.24	4.243	4.231	^{90}Zr	783.81	781.53	4.269	4.254	^{91}Zr	791.06	787.85	4.285	4.264
^{92}Zr	799.66	794.32	4.306	4.274	^{94}Zr	814.60	806.61	4.332	4.294	^{93}Nb	805.75	803.15	4.324	4.299
^{92}Mo	796.44	794.06	4.315	4.301	^{94}Mo	814.23	810.77	4.353	4.323	^{95}Mo	821.56	818.35	4.363	4.334
^{96}Ru	826.46	823.83	4.391	4.367	^{98}Ru	844.76	840.01	4.423	4.389					

width Δ of neutron induced reactions, as follows [16]:

$$E_0 \approx 0.172 T_9 \left(l + \tfrac{1}{2}\right) \text{MeV}, \tag{5}$$

$$\Delta \approx 0.194 T_9 \left(l + \tfrac{1}{2}\right)^{\frac{1}{2}} \text{MeV}. \tag{6}$$

Here, T_9 is the temperature in GK. Considering the typical temperature of stellar s-process sites, we have calculated the (n,γ) cross sections within the energy range of 1 keV to 1 MeV.

In the scenario of s-process nucleosynthesis, when a thermal equilibrium is achieved, the neutron spectrum corresponds to a Maxwell-Boltzmann distribution, and the Maxwellian-averaged cross sections are obtained by folding the total cross section at a particular energy with the thermalized neutron spectra over the wide range of neutron energy. It is defined as

$$\langle \sigma \rangle = \frac{2}{\sqrt{\pi}} \frac{\int_0^\infty \sigma(E_n) E_n \exp(-E_n/kT)\, dE_n}{\int_0^\infty E_n \exp(-E_n/kT)\, dE_n}. \tag{7}$$

Here E_n is the energy in the center-of-mass frame. Thus in principle, MACS should be close to $\sigma(E_n)$. The reaction rates in astrophysical scenarios can be obtained by folding the reaction cross sections with the Maxwell-Boltzmann distribution.

Nuclei, in the stellar interiors, not only exist in ground states but also in various excited states. For astrophysical applications, the rates have to be corrected for thermal excitations, which is taken care of by the stellar enhancement factor (SEF). This is defined as the ratio of the stellar rate relative to the ground-state rate [17],

$$\text{SEF} = \frac{\langle \sigma v \rangle_*}{\langle \sigma v \rangle_{\text{g.s.}}}. \tag{8}$$

Here, $\langle \sigma v \rangle_*$ is the reaction rate including excitations while $\langle \sigma v \rangle_{\text{g.s.}}$ is the reaction rate when the nuclei are in the ground state. The values of SEF for a range of energies can be found in the KADoNis database [18]. However, for nuclei close to the stability valley, it can be seen that the majority of the SEF values are 1.00 or very close to unity. Thus it is expected to be not very significant for the present case of study.

B. Relativistic mean-field model

The target radial matter densities used to fold the NN interaction are obtained from the RMF theory. The details of the RMF calculation are given in Ref. [4]. The point proton density ρ_p, obtained from the RMF theory, is folded with the standard Gaussian form factor $F(\mathbf{r})$ [4], to obtain the charge density $\rho_{\text{ch}}(\mathbf{r})$. The folding is done in coordinate space. The theoretical RMF density distribution, instead of experimental one, is used to give our model a complete and

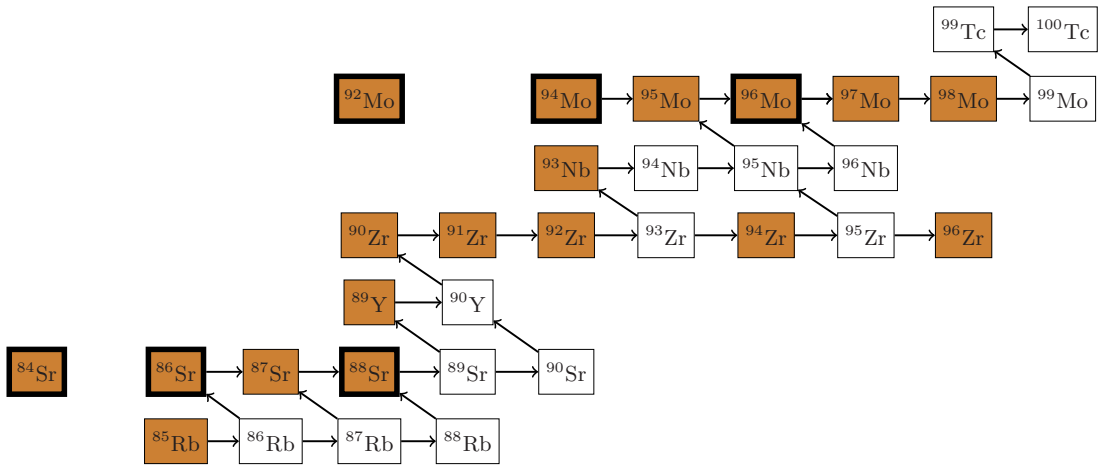

FIG. 2. The s-process path near the shell closure at $N = 50$. The colored rectangles represent stable and extremely long-lived isotopes. The p-nuclei and s-only isotopes are designated by rectangles with thick borders.

consistent theoretical approach. We have applied the same methodology throughout the earlier calculations of proton as well as neutron capture cross-section studies [4–11]. The theoretical densities can also supplement those regions where experimental information is unavailable, for example, regions far from stability valley, suitable for the r-process calculations. To investigate the feasibility of our RMF model, we have presented the binding energy and charge radius values and compared them with the available experimental data.

The difference between binding energies from the theoretical RMF approach and experimental data ($\Delta_{v\pi}$) is attributed to the strength of the n-p interaction of the nucleus and also to some extent to the odd-even mass difference, and a correction is done in this respect according to Ref. [21].

III. RESULTS

A. Relativistic mean-field results

Nuclear density is very important for the folding model prescription of the optical model potential. Hence, it is feasible to see the predictability of the theoretical RMF model. Experimental density distributions are available for a number of nuclei in this region of interest. In Fig. 1, we have plotted the theoretical density profiles for only two of them, for the sake of brevity, along with the experimental ones fitted with Fourier-Bessel parameters [22]. In Table I, the theoretical binding energy and charge radius values are listed with the measured values. Charge radius is the first moment of the nuclear charge distribution. Thus, the comparison of rms charge radii with experimental data can throw light on the quality of our theoretical RMF model. It can be easily seen that both our binding energy and charge radius values agree with the experimental values very well.

B. Neutron capture cross-section calculations

The nucleosynthesis path in the neighborhood of the shell closure at $N = 50$ is shown in Fig. 2. Figures 3–7 show the total (n,γ) cross sections for various targets in and around the $N = 50$ closed neutron shell for 1 keV to 1 MeV thermal energies. The experimental data, in general, are taken on the basis of the most recent measurements and also where a large number of data over a wide energy interval are available. All the experimental data are available at the web site of the National Nuclear Data Center [23].

Results for the (n,γ) cross sections for nuclei with $N = 46,48,49$ are shown in Fig. 3. Data for the p-nucleus ^{84}Sr are taken from Dillmann *et al.* [24]. They performed measurements at $kT = 25$ keV via an activation technique and reported an overall 5.7% error in their measurement with the major uncertainty coming from γ-ray intensity. Further, they extrapolated the cross sections at various thermal energies from 5 to 260 keV by normalizing the data with the values of different evaluated data libraries. The data for ^{85}Rb are from Ref. [25]. Bauer *et al.* [26] reported that cross sections for ^{86,87}Sr have to be known to an accuracy of 5% or better. They measured (n,γ) cross sections for these two isotopes for energies ranging from 100 eV to 1 MeV using a TOF facility and found strong resonance structures below 10 keV. Suitable corrections were made and no averaging over energy bins was

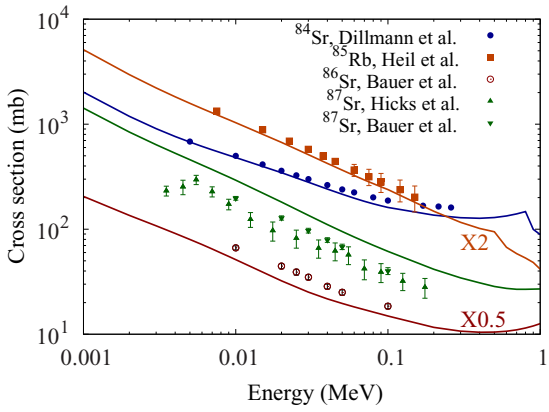

FIG. 3. Comparison of results of the present calculation (solid lines) with experimental measurements for ^{84}Sr [24], ^{85}Rb [25], ^{86}Sr [26], and ^{87}Sr [26,27], with $N = 46,48,49$. For the convenience of viewing, cross-section values for ^{85}Rb and ^{86}Sr have been multiplied by factors of 2 and 0.5, respectively.

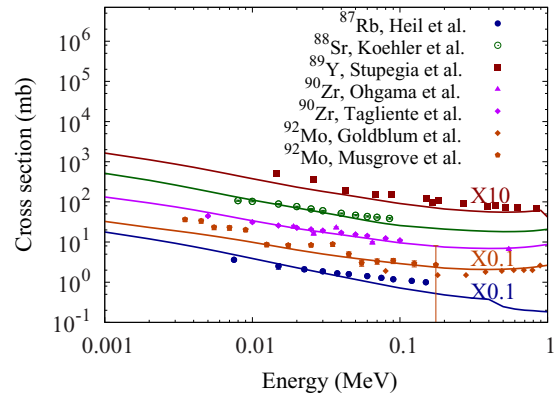

FIG. 4. Comparison of results of the present calculation (solid lines) with experimental measurements for ^{87}Rb [28], ^{88}Sr [29], ^{89}Y [28], ^{90}Zr [30,31], and ^{92}Mo [38,39], with $N = 50$. For the convenience of viewing, cross-section values for ^{87}Rb, ^{89}Y, and ^{92}Mo have been multiplied by factors of 0.1, 10, and 0.1, respectively.

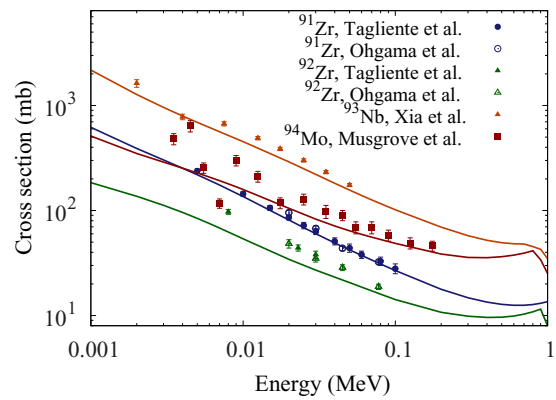

FIG. 5. Comparison of results of the present calculation (solid lines) with experimental measurements for ^{91}Zr [32,33], ^{92}Zr [32,34], ^{93}Nb [37], and ^{94}Mo [38], with $N = 51,52$.

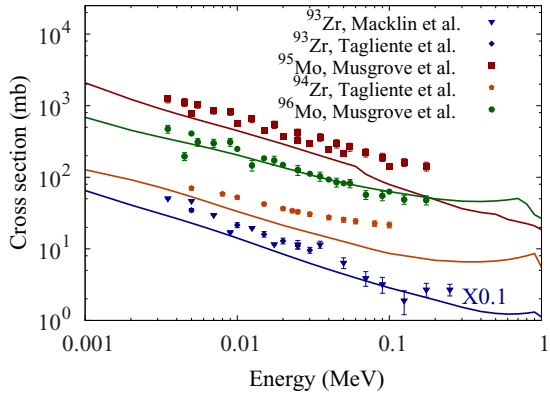

FIG. 6. Comparison of results of the present calculation (solid lines) with experimental measurements for ^{93}Zr [36], ^{95}Mo [38], ^{94}Zr [31], and ^{96}Mo [38], with $N = 53, 54$. For the convenience of viewing, cross-section values for ^{93}Zr have been multiplied by a factor of 0.1.

done by them. Their data decreases according to $1/v$ law above 20 keV. We have also plotted the data of Hicks *et al.* [27] for ^{87}Sr. We have plotted the recent measurements of Heil *et al.* [25] for ^{85,87}Rb.

Figures 4–7, show the cross sections for nuclei with $N = 50$; $N = 51,52$; $N = 53,54$; and $N = 55,56$, respectively. The abundant neutron magic ^{88}Sr has a very small cross section. Koehler *et al.* [29] recently improved the cross section for ^{88}Sr by a measurement with a wider neutron energy range and high resolution. They determined significant direct capture contributions and added them to the total MACS values. The data for ^{89}Y are taken from Ref. [28].

For ^{90,91,92}Zr, the data are from Refs. [30–34]. Tagliente *et al.* measured Maxwellian-averaged cross sections for several isotopes of zirconium with the improved n_TOF method. Experimental determination of small (n,γ) cross sections for ^{93}Zr is somewhat difficult due to its radioactive nature with a large β-decay half-life of about 1.53×10^6 years. This isotope is an important long-lived fission product. The sample of this isotope contains very poor enrichment. The experimental

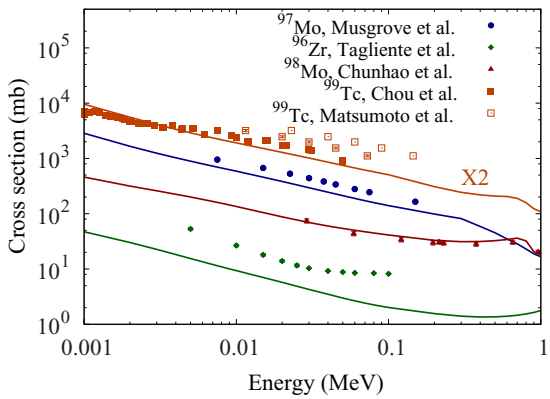

FIG. 7. Comparison of results of the present calculation (solid lines) with experimental measurements for ^{97}Mo [38], ^{96}Zr [31], ^{98}Mo [40], and ^{99}Tc [41,42], with $N = 55,56$. For the convenience of viewing, cross-section values for ^{99}Tc have been multiplied by a factor of 2.

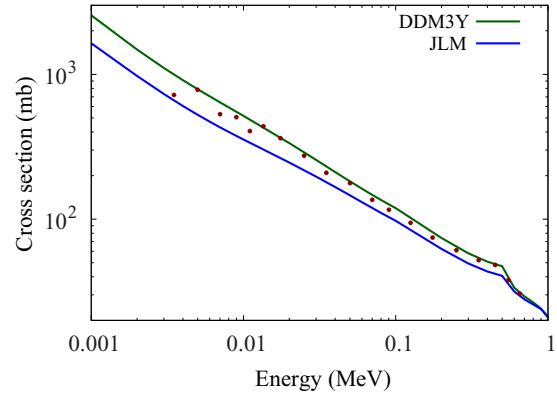

FIG. 8. Cross sections calculated with DDM3Y and JLM interactions compared with experimental data for ^{85}Rb.

values are taken from Refs. [35,36]. Macklin [35] derived the average neutron capture cross sections for this nucleus using the TOF technique from 3 to 300 keV. He identified 138 resonance peaks and further calculated the MACS for a range of thermal energies from 5 to 100 keV. The *s*-process may also contribute slightly to the production of ^{96}Zr, which, in general, is considered to be an *r*-only isotope [3], via the branching at ^{95}Zr at high neutron densities. The experimental data for ^{94}Zr and ^{96}Zr are from Ref. [31]. On average, our theory underpredicts the measurement of ^{96}Zr by a factor of ~ 3.

We have taken the cross sections for ^{93}Nb from Xia *et al.* [37]. The data for $^{92,94-97}$Mo are taken from Musgrove *et al.* [38]. They measured the cross sections by averaging over the energy bins from 3 to 90 keV with the high-resolution TOF technique. The measurements of Goldblum *et al.* [39] are also

TABLE II. Maxwellian-averaged cross sections at $kT = 30$ keV for nuclei near the $N = 50$ shell closure. Experimental values are from Ref. [18]. For unstable and radioactive nuclei, experimental data are not available. The nuclei with $N = 50$ are in bold.

	MACS (mb)				MACS (mb)		
Nucleus	Pres.	Expt.	MOST	Nucleus	Pres.	Expt.	MOST
$^{85}_{37}$Rb	259	234 ± 7	197	$^{86}_{37}$Rb	206		226
$^{87}_{37}$Rb	17.6	15.7 ± 0.8	18.8	$^{84}_{38}$Sr	283	300 ± 17	244
$^{86}_{38}$Sr	54.5	64 ± 3	51.0	$^{87}_{38}$Sr	139	92 ± 0.4	72.2
$^{88}_{38}$Sr	5.55	6.13 ± 0.11	5.02	$^{89}_{38}$Sr	17.6		22.0
$^{90}_{38}$Sr	7.02			**$^{89}_{39}$Y**	19.0	19 ± 0.6	16.6
$^{90}_{40}$Zr	18.4	19.3 ± 0.9	13.7	$^{91}_{40}$Zr	62.3	62.0 ± 3.4	53.7
$^{92}_{40}$Zr	28.1	30.1 ± 1.7	25.5	$^{93}_{40}$Zr	65.3	95 ± 10	67.8
$^{94}_{40}$Zr	17.4	26 ± 1	13.3	$^{95}_{40}$Zr	31.9		29.1
$^{96}_{40}$Zr	4.46	10.7 ± 0.5	10.7	$^{93}_{41}$Nb	224	266 ± 5	241
$^{94}_{41}$Nb	501		377	$^{95}_{41}$Nb	94.6		112
$^{92}_{42}$Mo	53.2	70 ± 10	45.5	$^{94}_{42}$Mo	87.2	102 ± 20	84.2
$^{95}_{42}$Mo	212	292 ± 12	237	$^{96}_{42}$Mo	113	112 ± 8	112
$^{97}_{42}$Mo	299	339 ± 14	276	$^{98}_{42}$Mo	73.8	99 ± 7	58.2
$^{99}_{42}$Mo	262		337	$^{99}_{43}$Tc	513	933 ± 47	423

TABLE III. MACS values from a few of other selected works at various energies listed with our results.

Nucleus	Energy (MeV)	Cross section (mb)		
		Present	Ref.	
^{85}Rb	0.025	290	234	[25]
^{87}Rb	0.012	33.8	26.3 ± 2.6	[48]
	0.020	23.4	19.5 ± 2.0	”
	0.030	17.6	15.5 ± 1.5	”
	0.040	14.3	13.4 ± 1.3	”
	0.050	12.2	12.4 ± 1.2	”
^{84}Sr	0.030	283	370 ± 17	[49]
^{86}Sr	0.030	54.5	57	[50]
	0.030	”	56.9	[18]
^{87}Sr	0.030	139	108 ± 20	[51]
^{88}Sr	0.025	6.22	6.72 ± 0.18	[52]
	0.030	5.55	5.6	[53]
	”	”	5.59	[18]
^{90}Zr	”	18.4	11 ± 3	[54]
^{91}Zr	”	62.3	59 ± 10	[54]
^{92}Zr	”	28.1	34 ± 6	”
^{94}Zr	”	17.4	21 ± 4	”
^{96}Zr	”	4.46	41 ± 12	”
^{99}Tc	”	513	782 ± 50	[55]
	”	”	779 ± 40	[56]

plotted for ^{92}Mo. The data for ^{98}Mo are from Chunhao *et al.* [40].

The experimental values for ^{99}Tc are from Refs. [41,42]. The most recent measurement has been done by Matsumoto *et al.* [42] with the TOF technique. They measured for incident neutron energies from 8 to 90 keV and at 190, 330, and 540 keV and obtained the results with an error of about 5%.

From the figures one can find that our calculations are quite reasonable over the entire range of interest. The folded microscopic optical potential, unlike the global or phenomenological potential, is highly sensitive to the nuclear structure or the properties of individual nucleons in the nucleus. This gives the advantage to the microscopic approach over the phenomenological approach. We have also performed the calculations with the semimicroscopic spherical nucleon-nucleus optical potential [43], which is calculated by folding the target radial matter density with the optical potential based on the work of Jeukenne, Lejeune, and Mahaux (JLM) [44–47], available in TALYS1.8 [12,13]. The differences in the cross sections are found to be from 5% to 35%, depending upon the reactions concerned. To show the difference, we have plotted both of them for only ^{85}Rb in Fig. 8.

In Table II, MACS values are presented along with experimental values, and theoretical values from MOST calculations. The experimental values are available at the KADoNis database [18], which is an updated version of the compilation by Bao *et al.* [57]. MOST calculations have been performed under the microscopic HF approach taking the JLM nucleon-nucleon interaction potential [43] into account. In Table III, we have also listed MACS values from some other selected theoretical and experimental works at various energies and compared them with our present results. The modern stellar codes on *s*-process nucleosynthesis demand MACS values at different energies rather than a single energy of 30 keV. Hence, in Table IV, we present MACS values at various thermal energies for nuclei containing the magic number ($N = 50$) of neutrons.

The *p*-process occurs at much higher temperature than the *s*-process. We have provided the reaction rates of three *p*-nuclei, as well as nuclei containing closed neutron shells, over a large range of stellar temperature in Table V. These rates are calculated considering the thermal excitations due to high stellar temperature. Moreover, for the sake of comparison, we have also listed the reaction rates available in the Brussels Nuclear Library for Astrophysics Applications (BRUSLIB) database [58]. These rates are obtained from calculations with the reaction code TALYS but with a different set of input parameters and a different optical model potential. The calculations of rates in the BRUSLIB database were performed with the nucleon-nucleus optical model potential of Ref. [59]

TABLE IV. MACS for ^{87}Rb, ^{88}Sr, ^{89}Y, ^{90}Zr, and ^{92}Mo. The experimental values are from Ref. [18].

Energy (MeV)	MACS (mb)									
	^{87}Rb		^{88}Sr		^{89}Y		^{90}Zr		^{92}Mo	
	Pres.	Expt.	Pres.	Expt.	Pres.	Expt.	Pres.	Expt.	Pres.	Expt.
0.005	63.6	111.2	18.0	10.88	64.7	68	52.7	44.4	144	277
0.010	38.6	63.2	11.3	11.86	40.3	40	34.2	31.3	96.4	158
0.015	28.7	48.1	8.63	9.88	30.8	30	26.9	25.8	76.6	115
0.020	23.4	40.3	7.16	8.21	25.6	25	22.8	22.7	65.5	93
0.025	19.9	35.7	6.22	7.02	22.3	21	20.2	20.7	58.4	79
0.030	17.6	32.4	5.55	6.13	19.0	19	18.4	19.3	53.2	70
0.040	14.3	27.7	4.67	5.04	16.7	16	15.8	17.1	46.2	59
0.050	12.2	23.6	4.12	4.35	14.7	14	14.1	15.5	41.6	53
0.060	10.8	22.0	3.73	3.95	13.2	13	13.0	14.3	38.3	49
0.080	8.87	18.4	3.25	3.25	11.3	11.3	11.4	11.4	34.0	45
0.100	7.67	15.2	2.96	3.36	10.5	10	10.5	11.0	31.4	43

TABLE V. Astrophysical reaction rates $N_A\langle\sigma v\rangle$ (cm ^{3}mol $^{-1}$s^{-1}) for a number of nuclei over a range of stellar temperature ($T_9 = 1$ GK). The rates are on the order of 10^5.

T_9	0.1	0.2	0.3	0.4	0.5	0.6	0.7	0.8	0.9	1.0	2.0	3.0	4.0	5.0
^{87}Rb[a]	33.46	28.58	26.19	24.66	23.55	22.71	22.05	21.51	21.06	20.68	18.28	17.29	16.88	15.14
^{87}Rb[b]	28.62	23.86	21.56	20.16	19.19	18.49	17.96	17.55	17.22	16.95	15.37	14.77	14.36	12.49
^{84}Sr[a]	416.47	408.68	409.28	413.43	419.64	427.06	435.23	443.92	453.03	462.52	579.25	716.42	755.28	376.64
^{84}Sr[b]	279.76	267.87	260.33	256.21	254.51	254.51	255.74	257.93	260.90	264.55	327.24	413.23	480.32	406.01
^{88}Sr[a]	9.71	8.67	8.20	7.94	7.78	7.70	7.66	7.66	7.68	7.73	8.71	10.22	12.17	14.12
^{88}Sr[b]	9.26	7.70	7.10	6.82	6.68	6.62	6.60	6.62	6.66	6.71	7.55	8.70	10.17	11.36
^{89}Y[a]	32.69	29.36	28.00	27.21	26.68	26.31	26.07	25.94	25.88	25.89	28.09	31.94	35.38	35.49
^{89}Y[b]	32.19	26.68	24.46	23.34	22.71	22.36	22.19	22.13	22.16	22.25	24.87	29.36	33.63	33.43
^{90}Zr[a]	29.16	27.28	26.75	26.53	26.46	26.48	26.59	26.77	27.02	27.32	32.05	39.12	49.01	61.04
^{90}Zr[b]	28.01	23.88	22.34	21.67	21.40	21.36	21.65	21.67	21.94	22.27	26.61	32.37	40.72	51.86
^{92}Mo[a]	81.74	77.99	77.25	77.24	77.47	77.89	78.49	79.24	80.13	81.15	96.18	117.75	145.49	160.11
^{92}Mo[b]	84.72	73.50	68.63	66.18	64.95	64.49	64.55	64.97	65.66	66.55	80.41	98.92	121.93	129.37
^{94}Mo[a]	130.40	126.39	126.14	126.81	127.78	128.98	130.42	132.07	133.92	135.95	163.01	194.86	187.38	95.455
^{94}Mo[b]	128.86	113.37	105.82	101.66	99.33	98.22	97.96	98.33	99.16	100.36	120.97	143.80	125.79	60.65

[a]Present work.
[b]Reference [58].

and QRPA + HFB calculations of the $E1$ γ-ray strength function [60].

The interaction of the nucleon with the nucleus is inherently complicated. In the spherical optical model, the interaction is represented by a one-body potential that depends only on the radial distance between the center of masses of nucleon and nucleus. However, the incident neutron is subject to various properties of the nucleus. Some of these effects are more pronounced for nuclei near the closed shells. Thus, a description with a single potential differs from one nucleus to another. Further, spherical symmetry is assumed in our model. As in the case of nuclei away from the closed shells, deformation gradually increases, so we expect some deviations. The isospin dependence and fine structure aspects of the NN interaction due to nuclear asymmetry can be another cause of deviation. Moreover, the mass region around Sr-Zr-Mo is subject to strong nuclear excitations. The interplay of single-particle and collective excitations results in the shape coexistence and rapid variation of structure with the changing nucleon numbers. This region of shape instabilities is very difficult to describe in a coherent and systematic way. Nevertheless, despite these shortcomings, the prediction of the cross sections, MACS values, and reaction rates from our model is quite reasonable and satisfactory.

IV. SUMMARY

In summary, we have constructed a semimicroscopic optical model potential to calculate astrophysically important (n,γ) reaction cross sections for energies ranging from 1 keV to 1 MeV, for nuclei in and around the $N = 50$ closed neutron shell. Standard DDM3Y NN interaction, folded with target matter densities, obtained from RMF theory is used. We have compared the results with the available experimental data. Our theory reproduces most of the measurements with reasonable agreement. The Maxwellian-averaged cross sections are calculated and presented with experimental measurements. The astrophysical reaction rates for some nuclei are also presented over a range of stellar temperature.

ACKNOWLEDGMENTS

The authors acknowledge financial support from the University Grants Commission (JRF and DRS), Department of Science and Technology (India), and the Alexander Von Humboldt Foundation (Germany).

[1] M. E. Burbidge, G. R. Burbidge, W. A. Fowler, and F. Hoyle, Rev. Mod. Phys. **29**, 547 (1957).
[2] A. G. W. Cameron, Astrophys. J. **130**, 452 (1959).
[3] F. Käppeler, H. Beer, and K. Wisshak, Rep. Prog. Phys. **52**, 945 (1989).
[4] S. Dutta, D. Chakraborty, G. Gangopadhyay, and A. Bhattacharyya, Phys. Rev. C **93**, 024602 (2016).
[5] C. Lahiri and G. Gangopadhyay, Phys. Rev. C **84**, 057601 (2011).
[6] C. Lahiri and G. Gangopadhyay, Eur. Phys. J. A **47**, 87 (2011).
[7] C. Lahiri and G. Gangopadhyay, Int. J. Mod. Phys. E **21**, 1250074 (2012).
[8] C. Lahiri and G. Gangopadhyay, Phys. Rev. C **86**, 047601 (2012).
[9] S. Dutta, D. Chakraborty, G. Gangopadhyay, and A. Bhattacharyya, Phys. Rev. C **91**, 025804 (2015).
[10] D. Chakraborty, S. Dutta, G. Gangopadhyay, and A. Bhattacharyya, Phys. Rev. C **91**, 057602 (2015).
[11] D. Chakraborty, S. Dutta, G. Gangopadhyay, and A. Bhattacharyya, Phys. Rev. C **94**, 015802 (2016).

[12] A. J. Koning, S. Hilaire, and M. Duizvestijn, in *Proceedings of the International Conference on Nuclear Data for Science and Technology, April 22–27, 2007, Nice, France*, edited by O. Bersillon, F. Gunsing, E. Bauge, R. Jacqmin, and S. Leray (EDP Sciences, Cedex, France, 2008), p. 211.
[13] http://www.talys.eu
[14] S. Goriely, S. Hilaire, and A. J. Koning, Phys. Rev. C **78**, 064307 (2008).
[15] R. Capote, M. Herman, P. Oblozinsky *et al.*, Nucl. Data Sheets **110**, 3107 (2009).
[16] R. V. Wagoner, Astrophys. J. Suppl. **18**, 247 (1969).
[17] C. Iliadis, *Nuclear Physics of Stars* (Wiley, New York, 2007).
[18] I. Dillmann, R. Plag, F. Käppeler, and T. Rauscher, KADoNiS v0.3 - The third update of the "Karlsruhe Astrophysical Database of Nucleosynthesis in Stars", in *EFNUDAT Fast Neutrons, Proceedings of the Scientific Workshop on Neutron Measurements, Theory, and Applications, 28–30 April 2009, Geel, Belgium*, edited by F.-J. Hambsch (Publications Office of the European Union, Luxembourg, 2010) p. 55; www.kadonis.org.
[19] M. Wang, G. Audi, A. H. Wapstra *et al.*, Chin. Phys. C **36**, 1603 (2012).
[20] I. Angeli, At. Data Nucl. Data Tables **87**, 185 (2004).
[21] G. Gangopadhyay, J. Phys. G **37**, 015108 (2010).
[22] H. De Vries, C. W. De Jager, and C. De Vries, At. Data Nucl. Data Tables **36**, 495 (1987).
[23] http://www.nndc.bnl.gov
[24] I. Dillmann, M. Heil, F. Käppeler, T. Rauscher, and F.-K. Thielemann, Phys. Rev. C **73**, 015803 (2006).
[25] M. Heil, F. Käppeler, E. Uberseder, R. Gallino, S. Bisterzo, and M. Pignatari, Phys. Rev. C **78**, 025802 (2008).
[26] R. W. Bauer, G. Bazan, J. A. Becker, R. E. Howe, and G. J. Mathews, Phys. Rev. C **43**, 2004 (1991).
[27] G. C. Hicks, B. J. Allen, A. R de L. Musgrove, and R. L. Macklin, Aust. J. Phys. **35**, 267 (1982).
[28] D. C. Stupegia, M. Schmidt, C. R. Keedy, and A. A. Madson, J. Nucl. Energy **22**, 267 (1968).
[29] P. E. Koehler *et al.*, Phys. Rev. C **62**, 055803 (2000).
[30] K. Ohgama, M. Igashira, and T. Ohsaki, AIP Conf. Proc. **819**, 373 (2006).
[31] G. Tagliente *et al.*, Phys. Rev. C **77**, 035802 (2008).
[32] K. Ohgama, M. Igashira, and T. Ohsaki, J. Nucl. Sci. Technol. **42**, 333 (2005).
[33] G. Tagliente *et al.*, Phys. Rev. C **78**, 045804 (2008).
[34] G. Tagliente *et al.*, Phys. Rev. C **81**, 055801 (2010).
[35] R. L. Macklin, Astrophys. Space Sci. **115**, 71 (1985).
[36] G. Tagliente *et al.*, Phys. Rev. C **87**, 014622 (2013).
[37] Y. Xia, Th. W. Gerstenhöfer, S. Jaag, F. Käppeler, and K. Wisshak, Phys. Rev. C **45**, 2487 (1992).
[38] A. R. de L. Musgrove, B. J. Allen, J. W. Boldeman, R. Macklin, and R. Winters, Nucl. Phys. A **270**, 108 (1976).
[39] B. L. Goldblum *et al.*, Phys. Rev. C **85**, 054616 (2012).
[40] W. Chunhao, Xia Yijun, Long Xianguan *et al.*, in *Nuclear Data for Science and Technology, Proceedings of an International Conference, Forschungszentrum Jülich, Germany, 13–17 May 1991*, edited by Syed M. Qaim (Springer, Berlin, 1992), p. 370.
[41] J. -C. Chou and H. Werle, J. Nucl. Energy **27**, 811 (1973).
[42] T. Matsumoto, M. Igashira, and T. Ohsaki, J. Nucl. Sci. Technol. **40**, 61 (2003).
[43] E. Bauge, J. P. Delaroche, and M. Girod, Phys. Rev. C **63**, 024607 (2001).
[44] J. P. Jeukenne, A. Lejeune, and C. Mahaux, Phys. Rep. **25C**, 83 (1976).
[45] J. P. Jeukenne, A. Lejeune, and C. Mahaux, Phys. Rev. C **10**, 1391 (1974).
[46] J. P. Jeukenne, A. Lejeune, and C. Mahaux, Phys. Rev. C **15**, 10 (1977).
[47] J. P. Jeukenne, A. Lejeune, and C. Mahaux, Phys. Rev. C **16**, 80 (1977).
[48] S. Jaag and F. Käppeler, Phys. Rev. C **53**, 2474 (1996).
[49] S. F. Mughabghab, *Atlas of Neutron Resonances: Resonance Parameters and Thermal Cross Sections Z = 1-100* (Elsevier Science, Amsterdam, Netherlands, 2006).
[50] M. Harris, Astrophys. Space Sci. **77**, 357 (1981).
[51] R. L. Macklin and J. H. Gibbons, Phys. Rev. **159**, 1007 (1967).
[52] F. Käppeler, W. Zhao, H. Beer, and U. Ratzel, Astrophys. J. **355**, 348 (1990).
[53] J. Boldeman, B. Allen, A. de L. Musgrove, and R. Macklin, Nucl. Phys. A **269**, 397 (1976).
[54] R. L. Macklin and J. H. Gibbons, Astrophys. J. **149**, 577 (1967).
[55] R. Winters and R. Macklin, Astrophys. J. **313**, 808 (1987).
[56] R. L. Macklin, Nucl. Sci. Eng. **81**, 520 (1982).
[57] Z. Y. Bao, H. Beer, F. Käppeler, F. Voss, and K. Wisshak, At. Data. Nucl. Data Tables **76**, 70 (2000).
[58] www.astro.ulb.ac.be/bruslib/
[59] A. J. Koning and J. -P. Delaroche, Nucl. Phys. A **713**, 231 (2003).
[60] S. Goriely, E. Khan, and M. Samyn, Nucl. Phys. A **739**, 331 (2004).